Radiotherapy and Oncology 138 (2019) 132–140

Contents lists available at ScienceDirect

Radiotherapy and Oncology

journal homepage: www.thegreenjournal.com

Original Article

MRI-guided mid-position liver radiotherapy: Validation of image processing and registration steps

T.N. van de Lindt, M.F. Fast, S.R. van Kranen, M.E. Nowee, E.P.M. Jansen, U.A. van der Heide, J.J. Sonke *

Department of Radiation Oncology, the Netherlands Cancer Institute, Amsterdam, the Netherlands

ARTICLE INFO

Article history:
Received 17 December 2018
Received in revised form 22 May 2019
Accepted 6 June 2019
Available online 25 June 2019

Keywords:
MRI-guidance
Liver SBRT
Mid-position
MR-linac
Image registration

ABSTRACT

Background & purpose: To propose a novel mid-position (midP) workflow for MRI-guided liver SBRT and provide a validation of the required midP-MRI generation and registration steps.
Materials & methods: The first step of the midP workflow is the generation of a simulation midP-MRI from a 4D-MRI scan using deformable image registration. Next, a planning midP-CT is warped to the midP-MRI to enable planning in the midP-MRI anatomy. For daily MRI-guidance, three different registration methods to the simulation midP-MRI are proposed; (1) 4D rigid registration of all phases of the daily 4D-MRI, (2) 3D rigid registration of the daily midP-MRI, and (3) 3D deformable registration of the daily midP-MRI. The midP-MRI image quality was assessed with respect to 4D-MRI acquisition time, which is related to over-sampling of the data acquisition (i.e. number of dynamics). The deformable registration precision for the midP-MRI generation was validated using the distance discordance metric (DDM). The deformable CT-MRI and daily MRI-MRI registration accuracies were quantified using the 'full circle method'.
Results: The DDM was 1.5 mm (median) within the liver, independent of the number of dynamics. The root-mean-squared difference between midP-MRIs based on 10 and 60 dynamics was only 5.2%. The full circle CT-MRI deformable registration error had a median 3D vector length of 1.8 mm in the liver. The daily MRI-MRI registration error was submillimeter for all three evaluated methods.
Conclusion: The feasibility of an MRI-guided mid-position workflow for liver SBRT is supported by the demonstrated high precision of all image processing and registration steps.
 Radiotherapy and Oncology 138 (2019) 132–140

Introduction

In recent years, the use of stereotactic body radiation therapy (SBRT) has led to substantial improvements in local control for primary and metastatic liver tumors [1–4]. The success of this treatment critically depends on accurate tumor localization, which is challenged by inter-fraction liver position variability and respiratory-induced liver motion [5]. Online motion and set-up correction strategies for liver SBRT on conventional linear accelerators (linacs), are currently based on the linac-integrated X-ray systems. These often require the implantation of fiducial markers due to poor tumor visibility [6] and can come at the expense of complications [7], patient discomfort and potential surrogacy errors [8]. The novel MRIdian (ViewRay Inc., Cleveland, OH, USA) and Unity (Elekta AB, Stockholm, Sweden) MR-linac systems provide in-room MRI-guidance. This enables direct daily tumor visibility, thus eliminating the invasive procedure of marker implantation.

There are various strategies to account for respiratory motion using image-guided liver radiotherapy [9]. In conventional linac-based liver SBRT, the internal target volume (ITV) method is widely used [10]. However, since the whole tumor trajectory of one breathing cycle is irradiated, the relatively large planning-target-volume (PTV) causes unnecessary damage to healthy tissue [9]. MRI-guided respiratory and breath-hold gating have recently been implemented clinically [11,12]. In this way the PTV is reduced, but beam delivery times are typically prolonged depending on the gating window and the regularity of breathing. Duty cycles can be improved using (voluntary) breath holds, but this requires patient compliance. For treatment with the mid-position (midP) strategy, the treatment plan is created on the time-weighted averaged anatomy of the patient [13,14]. In this way uncertainties due to respiratory motion are minimized while the patient is free-breathing. As the 3D motion of the tumor is incorporated as random error in the PTV margin, it results in a significantly smaller PTV compared to the ITV method (up to 40% for liver SBRT [15]) and comparable PTV size and coverage to exhale-gating [9], depending on tumor motion and tumor size. The midP strategy is relatively easy to implement as it only affects the treatment planning,

* Corresponding author.
E-mail address: j.sonke@nki.nl (J.J. Sonke).

https://doi.org/10.1016/j.radonc.2019.06.007
0167-8140/

however, at the same time it does not account for intra-fraction changes such as midP baseline drifts [5,16,17].

In today's midP liver SBRT workflow, a 4D-CT is acquired during simulation from which the midP planning-CT is created using deformable image registration [12,14]. For the online set-up correction, a 4D cone-beam (CB) CT is acquired and rigidly registered to the midP-CT based on the implanted markers [19]. We propose an MRI-guided mid-position workflow, where an additional simulation 4D-MRI is acquired of which a midP-MRI is generated and registered with the planning midP-CT. The daily 4D-CBCT is replaced with a 4D-MRI scan on the MR-linac (Fig. 1). Over the years, several 4D-MRI techniques for liver have been developed [20–27]. In general, slice based 4D-MRI methods are relatively easy to implement, as they are based on standard pulse sequences in combination with fast reconstruction algorithms. We previously developed a 4D-MRI method based on axial slices specifically for daily MRI-guidance of liver SBRT, providing direct tumor visibility [20].

In this study, an MRI-guided mid-position strategy for liver radiotherapy is proposed and all necessary image processing steps are validated. This includes an assessment of the precision and quality of the midP-MRI generation from 4D-MRI, deformable image registration between the simulation midP-CT and midP-MRI, and the image registration between the simulation and daily MRI.

Materials & methods

MRI-guided mid-position strategy

Fig. 1 shows a schematic overview of all the steps in the MRI-guided midP workflow. First, during simulation, a 4D-CT and a 4D-MRI are acquired of which a midP-CT and a midP-MRI are generated using deformable image registration. In analogy with the midP-CT generation [11,12], all phases of the 4D-MRI are registered to end-exhale using deformable image registration (Fig. 1A). The resulting deformation vector fields (DVFs) are averaged (M_{DVF}) and inverted (M_{DVF}^{-1}). All individual DVFs are then concatenated with M_{DVF}^{-1} and used to deform all phases to the mid-position. A final midP-MRI is derived by calculating the median intensity per voxel over the ten deformed phases.

To obtain the electron densities needed for treatment planning on the midP-MRI geometry, the midP-CT is deformed to the midP-MRI to create the planning midP-CT. The target and organs at risk are contoured and the plan is optimized on the deformed CT.

On the MR-linac, a daily pre-beam 4D-MRI is acquired for position verification and plan adaptation. We propose three methods for registration of the daily anatomy to the simulation midP-MRI (Fig. 1B):

- *4D rigid:* This is analogous to the method used in our CBCT-guided mid-position workflow. The ten phases of the daily 4D-MRI are rigidly registered to the simulation midP-MRI on the tumor. The time weighted average of the resulting translations (M_T) was calculated to get a shift-vector for daily plan adaption.
- *3D rigid:* A midP-MRI is generated from the daily 4D-MRI and rigidly registered to the simulation midP-MRI on the tumor to get a shift-vector for plan adaptation.
- *3D deformable:* A midP-MRI is generated and deformably registered to the simulation midP-MRI.

The resulting 4D and 3D rigid shift-vectors can be used in an adapt-to-position workflow [28]. In this workflow, the daily plan adaptation is performed based on a rigid tumor shift and the plan is re-optimized using the pre-treatment CT and contours with a shifted iso-center. The resulting DVFs from the 3D deformable method facilitate an adapt-to-shape workflow [28], in which the plan adaptation is optimized on the daily MRI geometry with adapted contours.

Data-sets

Volunteer data

Ten healthy volunteers underwent an MRI-examination on a 3 T MRI-scanner (Ingenia, Philips Healthcare, Best, The Netherlands), containing a slice-based 4D-MRI scan which was acquired and reconstructed as described by van de Lindt et al. [20]. The acquisition is based on a stack of axial 2D images covering the relevant field-of-view, which is acquired repeatedly (each full stack is referred to as 'dynamic'). A respiratory signal is retrieved from the acquired data and used to sort the images in 10 phase bins. If a bin remains empty due to under-sampling, the missing slice is interpolated. The following acquisition parameters were used: voxel size = $2 \times 2 \times 2$ mm^3, number of slices = 50, number of dynamics (D) = 60, total scan time = 15 min.

For each volunteer, the full 60 dynamics dataset was used to reconstruct a 4D-MRI scan (4D-MRI_{60}). Because 4D-MRI_{60} contains minimal missing data [20], midP-MRI_{60} was defined as the gold standard for the evaluation of the midP image quality. The first 50, 40, 30, 20 and 10 dynamics (equivalent acquisition times, Table S1) of the acquired data were also reconstructed into 4D-MRI scans, resulting in higher under-sampling [20]. The missing slices identified in the under-sampled 4D-MRI were removed from the gold standard 4D-MRI_{60} and interpolated, to create simulated 4D-MRI_D (D = 50,40,30,20,10) unbiased from variability in anatomical motion during the image acquisition. MidP-MRI_D (D = 50,40,30,20,10) was generated from the simulated 4D-MRI_D, to compare against midP-MRI_{60}.

Patient data

Three patients with liver metastases were imaged on the Unity (Elekta AB, Stockholm, Sweden) multiple times, before or after their treatment fractions on a conventional linac. Patient 1 had a liver sigmoid carcinoma metastasis (15 mm diameter) and underwent 4 MRI-examinations. Patient 2 had a rectum carcinoma metastasis (28 mm) and underwent 3 MRI-examinations. Patient 3 had two leiomyosarcoma metastases in the liver (9 and 7 mm) and also underwent 3 MRI-examinations. A retrospective self-sorting 4D-MRI scan [20] was acquired (voxel size = $2 \times 2 \times 5$ mm^3, slices = 25, D = 30, total scan time = 4:10 min) and midP-MRI_{30} scans were reconstructed. For each patient, a midP-CT was available, acquired with $1 \times 1 \times 3$ mm^3 voxel size on a 24-slice Somatom-Sensation-Open CT-scanner (Siemens, Forchheim, Germany).

Image registration

All deformable registrations were performed in Elekta's Advanced Medical Image Registration Engine (ADMIRE 2.0.1, Elekta AB, Stockholm, Sweden) using an NVIDIA Tesla K40c graphical processing unit (GPU) (2880 cores – 12 GB RAM). For intra-modality registrations, ADMIRE uses a deformable block-matching method with normalized-sum-of-squared-differences for robust initial alignment, followed by a dense non-linear image transformation using the local-cross-correlation-coefficient to align image details [29]. Inter-modality deformable registrations are performed using normalized mutual information.

All rigid registrations were performed using in-house developed software, using mutual information as cost function with a clipbox on the tumor area.

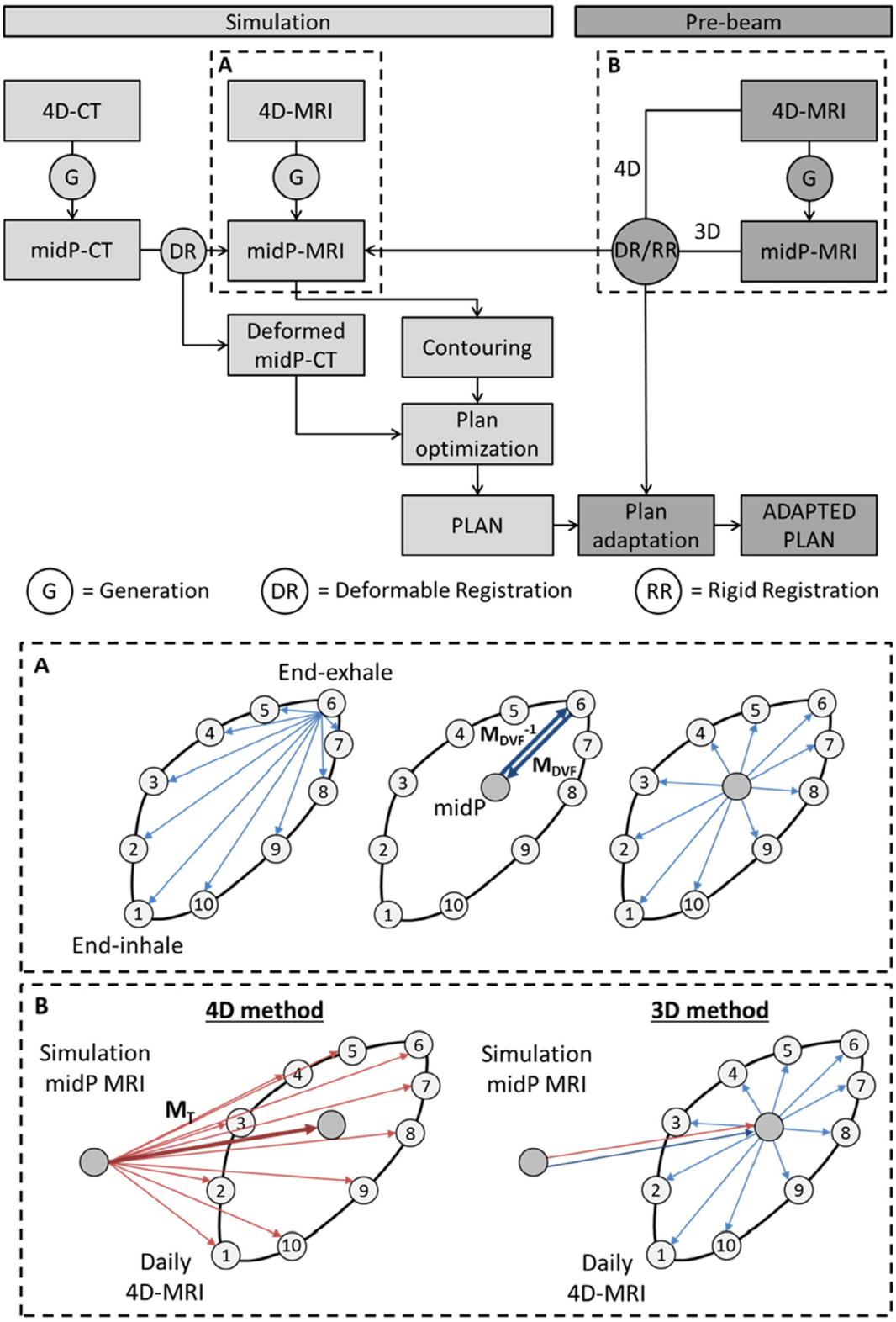

Fig. 1. Schematic overview of the MRI-guided midP workflow. (A) MidP generation from a 10 phase 4D-MRI. (B) Registration of the daily MRI to the simulation midP-MRI, with the blue arrows representing deformation vector fields and the red arrows representing rigid translations. In the 4D rigid method, all phases are rigidly registered to the simulation midP-MRI and the resulting translations are averaged (M_T). In the 3D method, a daily midP is generated and subsequently registered to the midP MRI, using rigid or deformable registration. (For interpretation of the references to color in this figure legend, the reader is referred to the web version of this article.)

MidP-MRI generation

The midP generation was performed with in-house developed software, using the DVFs generated in ADMIRE (Section "Image registration"). ADMIRE works on the discretized image grid when it performs the deformable registration, however, the physical plausibility constraints dictate that vectors do not usually point

directly from one voxel center to the center of another voxel. Instead, the DVFs from ADMIRE direct to continuous points in space. Because there is complimentary information in the ten 4D-MRI phases, the 4D-MRIs were deformed onto a finer $1 \times 1 \times 1$ mm^3 grid resulting in a high resolution midP-MRI.

The interpolated missing slices in the 4D-MRI scans were excluded from the midP-MRI generation to only include original data. This was done by first creating a binary 4D-MRI mask, setting all interpolated voxels to 1. Then, the DVFs were applied to the binary 4D-MRI mask, deforming the mask onto the $1 \times 1 \times 1$ mm^3 midP grid. All voxels with intensity >0.5 in the deformed mask, i.e. voxels that are dominated by initially interpolated missing data, were not taken into account when calculating the median from the 10 deformed midP images to create the final high resolution midP-MRI.

Validation

Deformable image registration for midP-MRI generation

The performance of the deformable registration method in the midP-MRI generation was evaluated using a modified version of the distance discordance metric (DDM) [30]. The DDM is a quantitative metric to evaluate the performance of deformable image registration in the absence of a ground truth. It is based on the variability in the DVFs, registering a given image to the reference imaging via different intermediate images.

All 10 4D-MRI phases were used to evaluate the DVF between end-inhale (phase 1) and end-exhale (phase 6). First, phase 1 was deformed to phase 6 via each of the other eight respiratory phases (Fig. 2A). For each voxel in phase 6, this resulted in eight originating positions in phase 1 of which then the centroid was calculated as an approximation of the unobservable ground truth location. The standard deviation (SD) of the distances to the centroid in left–right (LR), cranio-caudal (CC) and antero-posterior (AP) direction was calculated. From these a 3D vector length was derived, giving the DDM score for each voxel, with smaller values indicating better registration consistency. The DDM of 4D-MRI$_D$ (D = 60,50,40,30,20,10) was analyzed over all voxels of all volunteers within the liver and the body contour (incl. liver).

MidP-MRI image quality

The image quality of the midP-MRI was determined as a function of dynamics, over all volunteers. The root-mean-squared-difference (RMSD) and mean structural similarity (SSIM) index were calculated to evaluate the quality of the under-sampled midP-MRI$_D$ (D = 50,40,30,20,10) with respect to the fully sampled midP-MRI$_{60}$.

The RMSD is a widely used metric that provides a difference measure based on intensity differences relative to midP-MRI$_{60}$, and was evaluated over all voxels within the liver and within the body contour. Additionally, to quantify the visibility of structures (vessels) within the liver, the RMSD was evaluated over only the voxels with intensity $I < T_-$ or $I > T_+$ in the liver, where $T_\pm$ = mean ± SD intensity over all voxels in the liver.

The SSIM index [31] is a commonly used metric that predicts perceived quality difference of an image relative to a reference image, based on patterns of pixel intensities that were normalized for luminance and contrast. The SSIM index was computed within the liver and the body contour, between each slice in midP-MRI$_D$ (D = 50,40,30,20,10) and midP-MRI$_{60}$. The liver was manually contoured and the body contour was created with a threshold for analysis.

MidP-CT to midP-MRI deformable image registration

MidP-CT to midP-MRI deformable registration was evaluated with the 'full circle method', which has been shown to quantify the inter-modality registration precision in the absence of a ground-truth [32]. For a perfect registration algorithm, a circular

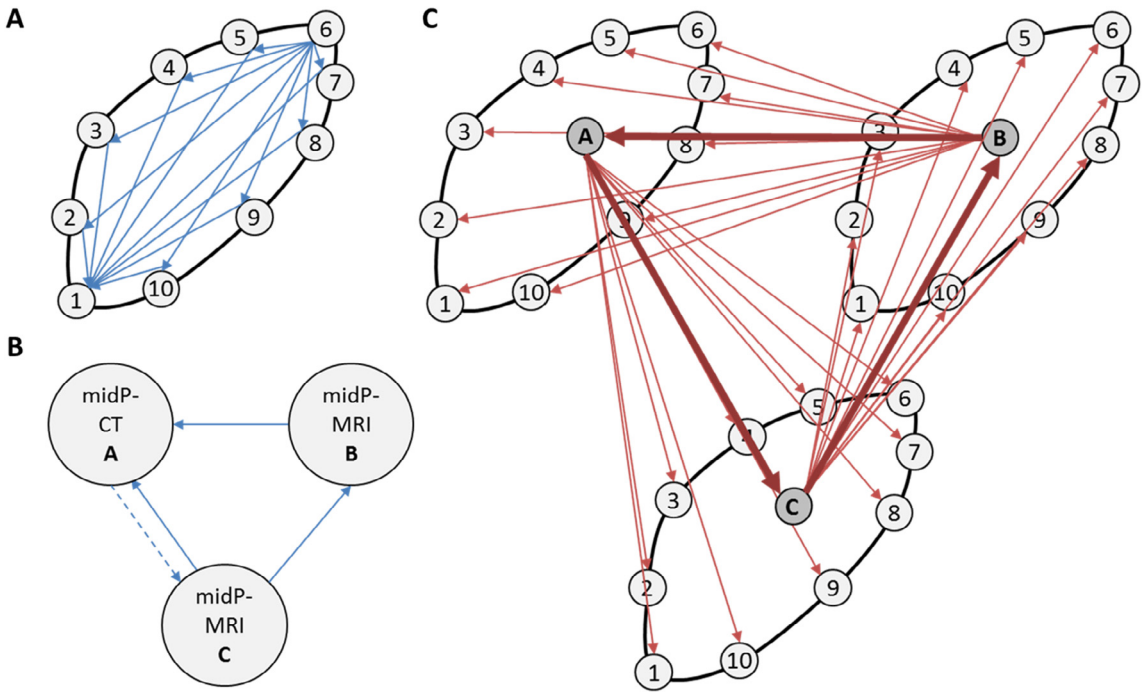

Fig. 2. (A) Deformation vector fields between end-inhale and exhale via all other 4D-MRI phases for the DDM analysis, to validate the deformable registration in the midP-MRI generation. (B) Deformation vector fields between a CT and two MRI scans in the full circle method, to validate the inter-modality deformable registration. (C) Rigid registrations between three 4D-MRI and midP-MRI scans in the full circle method, for validation of the daily 4D and 3D registration method. The blue arrows represent the deformation vector fields, the dashed arrow the inverse deformation vector field and the red arrows the rigid translations. (For interpretation of the references to color in this figure legend, the reader is referred to the web version of this article.)

concatenation of multiple registrations results in a zero total displacement. Imperfections, on the other hand, typically result in residual displacement following a full circle. To that end, for each patient, circular deformable registrations between a midP-CT and two midP-MRI scans were performed (Fig. 2B). The midP-CT was deformed to both midP-MRI scans and one of the DVFs was inverted to connect the DVFs in a circle. The residual vectors after concatenating the three resulting DVFs, corrected for the number of inter-modality deformations in one circle (division with $\sqrt{2}$), characterize the registration precision. All unique combinations of a midP-CT and two midP-MRI scans for each patient were analyzed, leading to a total of 12 circles (Supplements, Table S2). The residual vectors per voxel within the clinical liver and body contour were evaluated, with smaller residuals indicating better registration results.

To investigate the impact of registration error on CT-numbers, the corrected residual DVFs were applied to the midP-CT scans. Then, the difference between the original and distorted midP-CT was calculated and evaluated within the body contour and the liver.

Daily MRI to MRI registration

To validate the 4D rigid registration method between the daily 4D-MRI and the simulation midP-MRI, an adapted version of the full circle was applied [33] (Fig. 2C). Twelve unique circles (Supplements, Table 2S) of three image pairs each (a 4D-MRI and the corresponding midP-MRI) were created and the phases of 4D-MRI_A were rigidly registered to midP-MRI_B, 4D-MRI_B to midP-MRI_C and 4D-MRI_C back to midP-MRI_A. To validate the daily 3D rigid registration method, midP-MRIs were rigidly registered in a circle (Fig. 2C).

The 3D deformable method was validated with circular deformable registrations between three midP-MRI scans. Because in ADMIRE the concatenation of the forward and inverse registrations are constrained to zero, clockwise and counterclockwise circles provided identical results. Therefore, only six unique circles of three midP-MRI scans could be created (Supplements, Table 2S). Residuals were corrected for the number of intra-modality registrations ($\sqrt{3}$) and analyzed within the body contour and the liver.

Results

Volunteer and patient midP-MRIs were reconstructed from the 4D-MRI scans (Figs. 3 and 4). The total computation time of 10 DVFs of 25–50 slices per respiratory phase in ADMIRE was approximately 30–40 s. Volunteer median (interquartile range) respiratory period derived from the self-sorting signal and peak-to-peak CC diaphragm amplitude derived from the 4D-MRI scans were 4.5 (4.0–5.2) s and 7 (5–12) mm. Patient respiratory period and tumor motion in CC were 4.0 (3.7–5.7) s and 8 (5–10) mm.

In general, by combining the information of all 10 respiratory phases in the midP-generation, 4D-MRI artefacts were reduced and tumor visibility was improved (Figs. 3 and 4). Fig. 4 shows that sorting artefacts were mitigated in the midP-MRI scans compared to the inhale and exhale phases of the 4D-MRI scans. This is especially visible in the sagittal and coronal planes of patient C, where sorting artifacts were clearly present at the top of the non-smooth diaphragm in the inhale phase. Liver lesions were visible in all patient midP-MRI scans (Fig. 4). The small 7 mm lesion in patient C was not visible in all respiratory phases of the 4D-MRI (Fig. 4C, inhale, axial), but could be detected in the midP-MRI (Fig. 4C, midP, axial).

The amount of missing data in the 4D-MRI reconstructions increased with decreasing number of dynamics as expected (Fig. 5A). However, this did not deteriorate the performance of the deformable registration in the midP generation (Fig. 5B). The DDM was stable over the number of dynamics, with an average median (interquartile range) of 0.9 (0.4–1.8) mm within the body contour and 1.5 (0.9–2.7) mm within the liver. The right panel in Fig. 3 shows that larger DDM values (>3 mm) were found in areas that are affected by cardiac or gastrointestinal motion such as the heart, stomach and bowel.

Stable image quality of the midP-MRI was shown, even for highly under-sampled 4D-MRI. The RMSD in the liver was largest for 10 dynamics with a median (interquartile range) of 5.2 (4.8–6.6) % over all volunteers (Fig. 5C). The RMSD of the vessels in the liver increased to a maximum of 11.6 (9.8–13.5) % for 10 dynamics with respect to 60 dynamics. The SSIM between

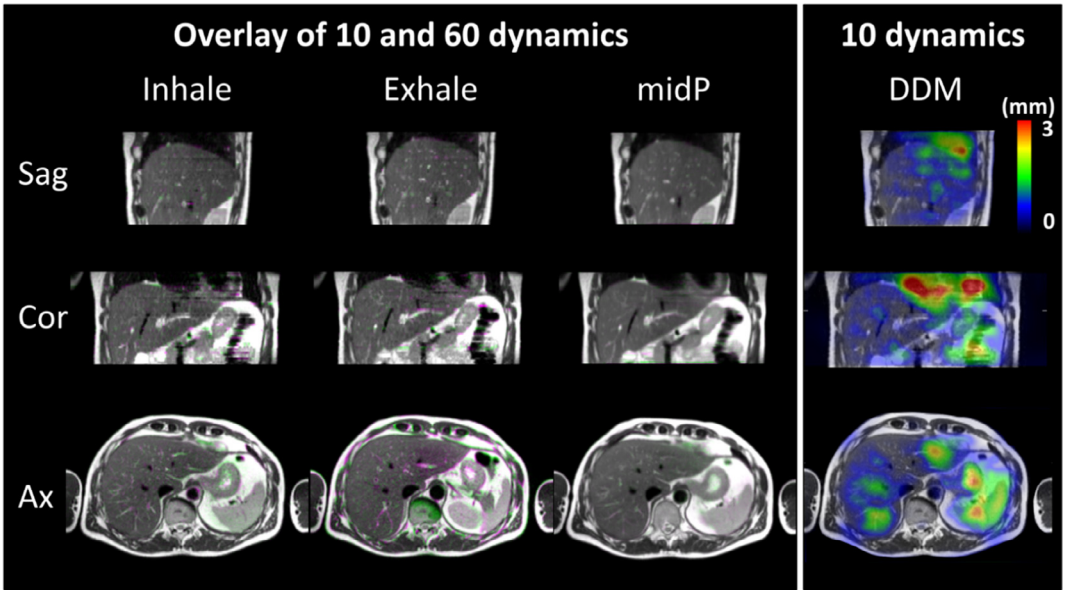

Fig. 3. Sagittal (Sag), coronal (Cor) and axial (Ax) representation of a volunteer 4D-MRI inhale and exhale phase and reconstructed midP-MRI, with green-purple overlay of images generated from 10 and 60 dynamics. More green-purple is present in the inhale and exhale images, compared to the midP images. This means there are larger differences between 10 and 60 dynamics based individual 4D-MRI phases compared to the midP. On the left plane, a 10 dynamics inhale phase with corresponding DDM values is shown.

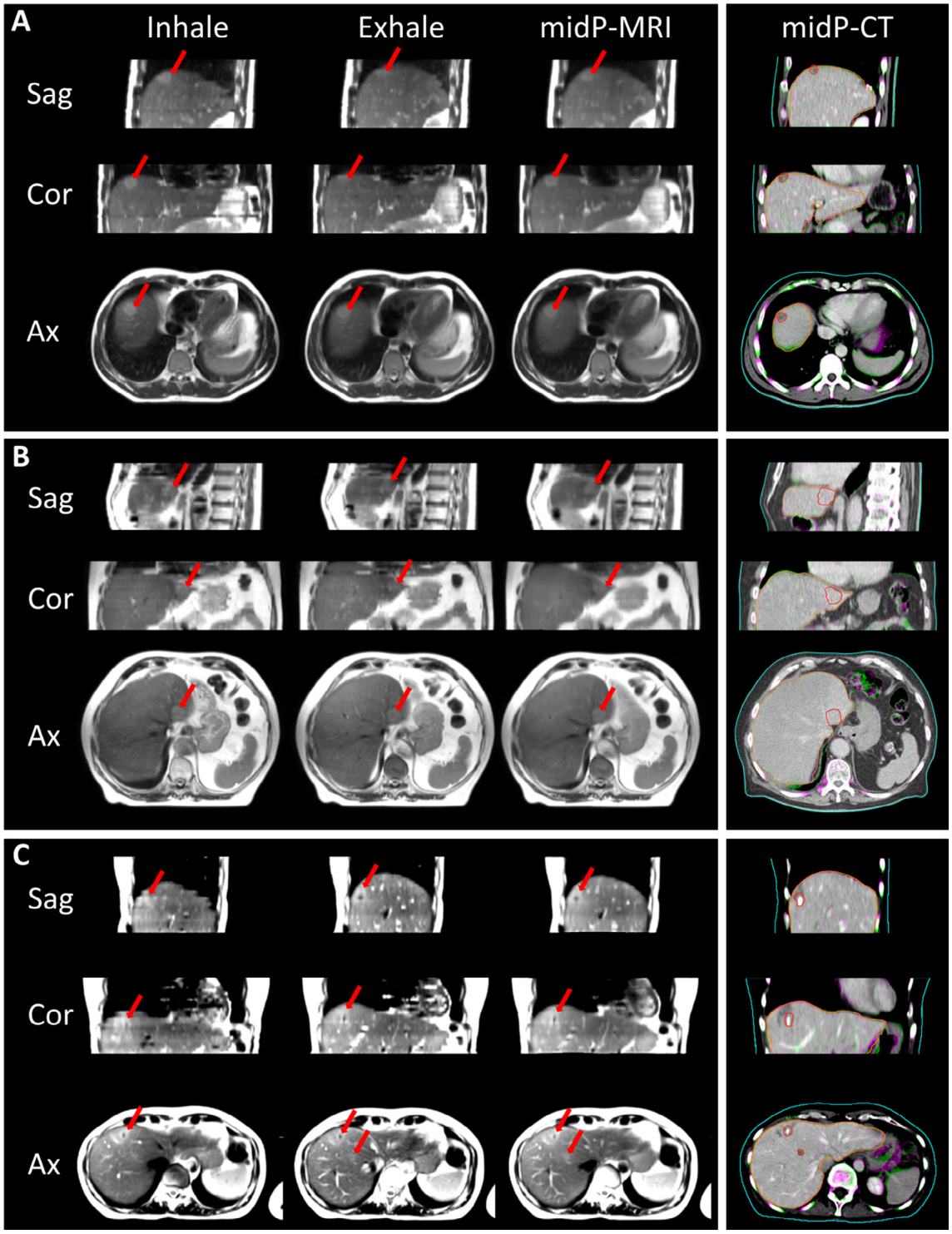

Fig. 4. Sagittal (Sag), coronal (Cor) and axial (Ax) representation of three patients through the center of the (largest) lesion. Left: The inhale and exhale phase of a 4D-MRI and reconstructed midP-MRI scans are presented. The visible tumor area is indicated with a red arrow. Right: A green-purple overlay of the original and distorted CT scan resulting from the inter-modality full circle deformable registration validation, which show minimal differences. The GTV (red), liver (orange) and external (blue) contours are shown on the CT. (For interpretation of the references to color in this figure legend, the reader is referred to the web version of this article.)

midP-MRI$_D$ (D = 50,40,30,20,10) and midP-MRI$_{60}$ decreased with decreasing number of dynamics (Fig. 5D). However, all SSIM values were high; even for 10 dynamics the median over all volunteers was 0.98 (0.97–0.98) in the liver and 0.97 (0.96–0.98) inside the body contour. The green-purple overlay in Fig. 3 shows larger differences due to under-sampling between 4D-MRI$_{10}$ and gold standard 4D-MRI$_{60}$, compared to midP-MRI$_{10}$ and midP-MRI$_{60}$.

Results of the inter-modality deformable registration full circle method are shown in Table 1A. The registration error had minimal impact on the CT number, with a 5–95th percentile of −62 to 65 HU within the body contour and −31 to 36 HU in the liver. This is also shown in the right panel of Fig. 4 by the minimal differences between the original and distorted CT.

The results of the daily 4D and 3D rigid, and 3D deformable full circle method are shown in Table 1B and C. The rigid methods had

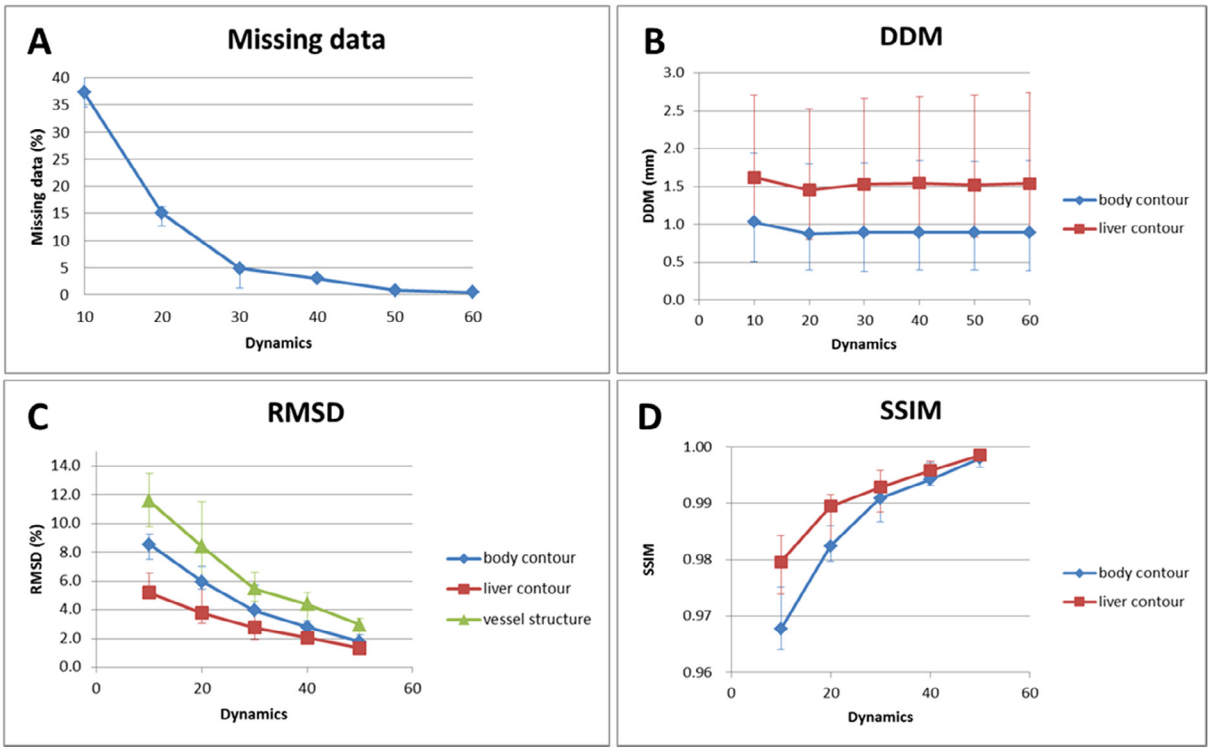

Fig. 5. (A) Missing data and (B) DDM calculated from DVFs between respiratory phases, of 4D-MRI$_D$ (D = 60,50,40,30,20,10). (C) RMSD and (D) SSIM of midP-MRI$_D$ (D = 50,40,30,20,10) with respect to midP-MRI$_{60}$. Median, 25th and 75th percentiles (whiskers) over all voxels in body and liver contour of 10 volunteers are shown.

Table 1
Full circle registration results. Median (interquartile range) of residual errors over all evaluated circles.

(A) Deformable midP-CT to midP-MRI registration and impact on CT number

		In body contour	In liver contour
LR	(mm)	0.0 (−0.5 – 0.5)	0.0 (−0.6 – 0.6)
CC	(mm)	0.0 (−1.0 – 1.0)	0.0 (−1.0 – 1.0)
AP	(mm)	0.1 (−0.4 – 0.6)	0.3 (−0.3 – 1.0)
3D vector length	(mm)	1.6 (1.0 – 2.7)	1.8 (1.2 – 2.8)
CT number	(HU)	0 (−11 – 12)	0 (−8 – 9)

(B) 4D and 3D rigid daily MRI-MRI registration

		4D method	3D method
LR	(mm)	0.2 (−0.1 – 0.3)	0.1 (−0.2 – 0.3)
CC	(mm)	0.8 (0.4 – 1.1)	0.2 (−0.0 – 0.4)
AP	(mm)	−0.4 (−0.6 – −0.2)	−0.3 (−0.5 – 0.4)
3D vector length	(mm)	0.9 (0.7 – 1.2)	0.7 (0.5 – 1.0)

(C) 3D deformable daily MRI-MRI registration

		In body contour	In liver contour
LR	(mm)	0.0 (−0.2 to 0.2)	0.0 (−0.2 to 0.2)
CC	(mm)	0.0 (−0.4 to 0.4)	0.0 (−0.3 to 0.6)
AP	(mm)	0.0 (−0.2 to 0.2)	0.0 (−0.3 to 0.2)
3D vector length	(mm)	0.7 (0.3 to 1.6)	0.7 (0.3 to 1.7)

comparable precision with submillimeter median vector lengths, dominated by the error in CC direction. The median residuals of the deformable method were submillimeter in the liver as well as the body contour. As for patient A more 4D-MRI scans were available, the full circle method for patient A contained more circles than for patients B and C (Supplements, Table S2). Therefore, we performed the full circle analyses again with three 4D-MRIs for each patient (excluding the fourth 4D-MRI of patient A). This had negligible impact on the full circle method results.

Discussion

We proposed an MRI-guided mid-position workflow for liver radiotherapy on an MR-linac and validated all necessary image processing and registration steps. This approach has the potential to eliminate the need for the time-consuming and invasive marker implantation of conventional image-guided liver SBRT. The proposed workflow has been shown to be feasible and accurate.

The midP-MRI generation presented in this paper was inspired by the original midP-CT method by Wolthaus et al. [13]. The original method was adapted to account for missing slices due to under-sampling of the 4D-MRI data. Missing data were excluded from the final midP-MRI such that the missing information in one phase could be substituted with complementary information from any of the other respiratory phases. This resulted in stable image quality of the midP-MRI regardless of the number of dynamics. Even for high under-sampling with the acquisition of only 10 dynamics, the median RMSD in the liver was 5.2% and the SSIM 0.98 relative to the gold standard of 60 dynamics. The average SSIM for individual 10 dynamics 4D-MRI phases compared to 60 dynamics found by van de Lindt et al. [20] was lower (∼0.86). This corresponds with our visual perception of the images (Fig. 3), which show that the differences between 4D-MRI phases based on 10 or 60 dynamics are larger than the differences in the corresponding midP-MRI scans. The deformable registration precision in the midP-MRI generation was also stable over the number of dynamics with average median DDM values of 0.9 mm and 1.5 mm within the body and liver contour, respectively. This is in the same order of magnitude as the average registration error in the liver midP-CT generation of mean(±SD) 1.8(±0.5) mm found by Kruis et al. [14].

To register the planning midP-CT with the simulation midP-MRI for treatment planning, inter-modality deformable registration is required. This was validated using the full circle method [32], with

a median midP-CT to midP-MRI registration precision of 1.6 mm in the body contour and 1.8 mm in the liver. This is an upper limit of the registration error, since the full circle includes the intra-modality midP-MRI registration error which was not corrected for. In 2010, a multi-institution study of three MRI to CT deformable registration algorithms was performed [34]. Average absolute errors reported were in the same order of magnitude: 1.1–2.6 mm (LR), 2.0–5.0 mm (AP), and 2.2–2.6 mm (CC). The ADMIRE algorithm for intra-patient deformable MRI registrations has previously been investigated [35] using the scale-invariant feature transform (SIFT), reporting average random errors between 1.5 and 1.8 mm. The inter-modality registration error had minimal impact on the CT numbers, hinting at a minimal impact on dose calculations.

The 4D and 3D registration of the daily 4D-MRI and simulation midP-MRI, acquired for the purpose of daily plan adaptation, were evaluated using the full circle method. This resulted in comparable submillimeter registration precision, which can be accounted for in the treatment margin [36]. The rigid registration in the 4D method is fast (order of seconds), compared to the additional deformable registrations in the 3D method (30–40 s). However, manually checking and possibly adjusting the ten rigid registrations may also be time-consuming. We showed that the midP-MRI provides better image quality than the individual 4D-MRI phases and mitigates the 4D-MRI artifacts, which makes the subsequent registration easier. In patient C (Fig. 4C), the smallest lesion was not visible in all respiratory phases but it could be detected in the midP-MRI. The midP-MRI, being a single 3D image, is potentially easier to integrate into the daily plan adaptation workflow. The resulting 4D and 3D rigid shift-vectors can be used in an adapt-to-position workflow [28]. This method is based on a rigid tumor shift and does not take into account anatomical changes of the tumor or OARs. The 3D deformable method can facilitate an adapt-to-shape workflow [28], which accounts for contour deformations. For the latter, it is important that the accuracy of the contour propagation of the tumor and OARs are further investigated, especially since the DDM analysis of the MRI to MRI registration showed larger errors (>3 mm) in areas such as the heart, stomach and bowel, probably due to cardiac and gastrointestinal motion and resulting motion artifacts in the 4D-MRI scan. The bowel may also contain (dis)appearing air cavities, which presents a challenge for deformable registration. A daily adaptation based on deformable registration requires a relatively large FOV covering all relevant OARs, at the cost of acquisition time.

The registration and image quality metrics used in this study have some limitations. The SSIM and RMSD are global metrics which can be dominated by the homogenous tissue in the liver and slightly underestimate the error in other structures such as the vessels and the tumor. Therefore, the RMSD was additionally analyzed on only the vessel structure in the liver. However, this introduces the risk of overestimation of the actual error due to the large impact of small geometrical displacements. The DDM was based on the variability in the distance between corresponding voxels from different images which are co-registered to the same voxel in a reference image. In principle, low values indicate accurate registration and high values a poor registration. However, the metric is susceptible to systematic failure due to the lack of a ground truth [30]. In the full circle method, where three registrations are concatenated in a circle, there is also a possibility that errors cancel each other out. Due to the limited patient data available, the unique circles were grouped and assumed to be independent.

The midP strategy was demonstrated in combination with the axial self-sorting 4D-MRI method [20], but can in principle be used in combination with any 4D-MRI technique. When used in combination with amplitude-binned 4D-MRI [21], the non-uniformity in the time spend per bin needs to be accounted for in the midP generation by applying a weighted median [18]. Voxels that were dominated by initially interpolated missing data, were not taken into account when calculating the median from the 10 deformed midP images to create the final high resolution midP-MRI. The threshold for exclusion can be set to the user's preference, for example if the threshold of 0.5 results in voxels in the midP without information. There is a well-known trade-off in MRI of the image acquisition time and spatial resolution. Mapping the midP-MRI to a finer grid, enables the user to acquire the 4D-MRI with a larger voxel size to speed up the 4D-MRI acquisition. This is especially relevant for daily 4D-MRI, to minimize the overall treatment time slots.

As described in literature, the time-averaged tumor position can change over time [5,16,17]. However, the proposed midP workflow does not compensate for these intra-fraction position changes. In the future, the midP strategy on the MR-linac can be extended with tumor trailing in which the shape of the beam aperture is adapted according to slow baseline drifts of the tumor [37]. The next step before implementation of MRI-guided mid-position treatments in our clinic is to validate the geometric and dosimetric accuracy of the method using phantom measurements on the Unity MR-linac.

Declaration of Competing Interest

None.

Acknowledgement

We would like to thank Celia Juan de la Cruz (NKI-AVL) for implementing the distance discordance metric (DDM).

Appendix A. Supplementary data

Supplementary data to this article can be found online at https://doi.org/10.1016/j.radonc.2019.06.007.

References

[1] Joo JH, hong Park J, Kim JC, Yu CS, Lim SB, Park IJ, Kim TW, Hong YS, pyo Kim K, Yoon SM, Park J, Kim JH. Local control outcomes using stereotactic body radiation therapy for liver metastases from colorectal cancer. Int J Radiat Oncol Biol Phys 2017;99:876–83.
[2] McPartlin A, Swaminath A, Wang R, Pintilie M, Brierley J, Kim J, et al. Long-term outcomes of phase 1 and 2 studies of SBRT for hepatic colorectal metastases. Int J Radiat Oncol Biol Phys 2017;99:388–95.
[3] Klement RJ, Guckenberger M, Alheid H, Allgäuer M, Becker G, Blanck O, et al. Stereotactic body radiotherapy for oligo-metastatic liver disease – influence of pre-treatment chemotherapy and histology on local tumor control. Radiother Oncol 2017;123:227–33.
[4] Ohri N, Tomé WA, Méndez Romero A, Miften M, Ten Haken RK, Dawson LA, et al. Local control after stereotactic body radiation therapy for liver tumors. Int J Radiat Oncol Biol Phys 2018.
[5] Case RB, Sonke JJ, Moseley DJ, Kim J, Brock KK, Dawson LA. Inter- and intrafraction variability in liver position in non-breath-hold stereotactic body radiotherapy. Int J Radiat Oncol Biol Phys 2009;75:302–8.
[6] Seppenwoolde Y, Wunderink W, Van Veen SRW, Storchi P, Romero AM, Heijmen BJM. Treatment precision of image-guided liver SBRT using implanted fiducial markers depends on marker-tumour distance. Phys Med Biol 2011;56:5445–68.
[7] Park SH, Won HJ, Kim SY, Shin YM, Kim PN, Yoon SM, et al. Efficacy and safety of ultrasound-guided implantation of fiducial markers in the liver for stereotactic body radiation therapy. PLoS One 2017;12.
[8] Wunderink W, Méndez Romero A, Seppenwoolde Y, De Boer H, Levendag P, Heijmen B. Potentials and limitations of guiding liver stereotactic body radiation therapy set-up on liver-implanted fiducial markers. Int J Radiat Oncol Biol Phys 2010;77:1573–83.
[9] Wolthaus JWH, Sonke JJ, van Herk M, Belderbos JSA, Rossi MMG, Lebesque JV, et al. Comparison of different strategies to use four-dimensional computed tomography in treatment planning for lung cancer patients. Int J Radiat Oncol Biol Phys 2008;70:1229–38.
[10] Benedict SH, Yenice KM, Followill D, Galvin JM, Hinson W, Kavanagh B, et al. Stereotactic body radiation therapy: the report of AAPM Task Group 101. Med Phys 2010.

[11] Wojcieszynski AP, Rosenberg SA, Brower JV, Hullett CR, Geurts MW, Labby ZE, et al. Gadoxetate for direct tumor therapy and tracking with real-time MRI-guided stereotactic body radiation therapy of the liver. Radiother Oncol 2016;118:416–8.
[12] Henke L, Kashani R, Robinson C, Curcuru A, DeWees T, Bradley J, et al. Phase I trial of stereotactic MR-guided online adaptive radiation therapy (SMART) for the treatment of oligometastatic or unresectable primary malignancies of the abdomen. Radiother Oncol 2018;126:519–26.
[13] Wolthaus JWH, Sonke JJ, Van Herk M, Damen EMF. Reconstruction of a time-averaged midposition CT scan for radiotherapy planning of lung cancer patients using deformable registration. Med Phys 2008;35:3998–4011.
[14] Kruis MF, Van De Kamer JB, Sonke JJ, Jansen EPM, Van Herk M. Registration accuracy and image quality of time averaged mid-position CT scans for liver SBRT. Radiother Oncol 2013;109:404–8.
[15] Velec M, Moseley JL, Brock KK. Simplified strategies to determine the mean respiratory position for liver radiation therapy planning. Pract Radiat Oncol 2014;4:160–6.
[16] Liang Z, Liu H, Xue J, Hu B, Zhu B, Li Q, et al. Evaluation of the intra- and interfractional tumor motion and variability by fiducial-based real-time tracking in liver stereotactic body radiation therapy. J Appl Clin Med Phys 2018.
[17] Cusumano D, Dhont J, Boldrini L, Chiloiro G, Teodoli S, Massaccesi M, et al. Predicting tumour motion during the whole radiotherapy treatment: a systematic approach for thoracic and abdominal lesions based on real time MR. Radiother Oncol 2018;129:456–62.
[18] Kruis MF, Van De Kamer JB, Belderbos JSA, Sonke JJ, Van Herk M. 4D CT amplitude binning for the generation of a time-averaged 3D mid-position CT scan. Phys Med Biol 2014;59:5517–29.
[19] Sonke JJ, Zijp L, Remeijer P, Van Herk M. Respiratory correlated cone beam CT. Med Phys 2005;32:1176–86.
[20] van de Lindt TN, Fast MF, van der Heide UA, Sonke JJ. Retrospective self-sorted 4D-MRI for the liver. Radiother Oncol 2018;127:474–80.
[21] van de Lindt T, Sonke JJ, Nowee M, Jansen E, van Pelt V, van der Heide U, et al. A self-sorting coronal 4D-MRI method for daily image guidance of liver lesions on an MR-LINAC. Int J Radiat Oncol Biol Phys 2018;102:875–84.
[22] Zhou Z, Cao M, Sheng K, Yang Y, Hu P, Han F. Respiratory motion-resolved, self-gated 4D-MRI using rotating cartesian k-space (ROCK). Med Phys 2017;44:1359–68.
[23] Paganelli C, Summers P, Bellomi M, Baroni G, Riboldi M. Liver 4DMRI: a retrospective image-based sorting method. Med Phys 2015;42:4814–21.
[24] Liu Y, Yin FF, Chen NK, Chu ML, Cai J. Four dimensional magnetic resonance imaging with retrospective k-space reordering: a feasibility study. Med Phys 2015;42:534–41.
[25] Von Siebenthal M, Székely G, Gamper U, Boesiger P, Lomax A, Cattin P. 4D MR imaging of respiratory organ motion and its variability. Phys Med Biol 2007;52:1547–64.
[26] Mickevicius NJ, Paulson ES. Investigation of undersampling and reconstruction algorithm dependence on respiratory correlated 4D-MRI for online MR-guided radiation therapy. Phys Med Biol 2017;62:2910–21.
[27] Li D, Tuli R, Sharif B, Pang J, Yue Y, Deng Z, et al. Four-dimensional MRI using three-dimensional radial sampling with respiratory self-gating to characterize temporal phase-resolved respiratory motion in the abdomen. Magn Reson Med 2015;75:1574–85.
[28] Winkel D, Bol GH, Kroon PS, van Asselen B, Hackett SS, Werensteijn-Honingh AM, et al. Adaptive radiotherapy: the Elekta unity MR-linac concept. Clin. Transl. Radiat. Oncol. 2019:1–6.
[29] Pennec X, Ayache N, Roche A, Cachier P. Non-rigid MR/US registration for tracking brain deformations. In: Proceedings – International Workshop on Medical Imaging and Augmented Reality, MIAR 2001. p. 79–86.
[30] Saleh ZH, Apte AP, Sharp GC, Shusharina NP, Wang Y, Veeraraghavan H, et al. The distance discordance metric – A novel approach to quantifying spatial uncertainties in intra- and inter-patient deformable image registration. Phys Med Biol 2014;59:733–46.
[31] Wang Z, Bovik AC, Sheikh HR, Simoncelli EP. Image quality assessment: from error visibility to structural similarity. IEEE Trans Image Process 2004;13:600–12.
[32] van Herk M, Touw A, Muller S, Rasch C, de Munck JC, Lebesque JV. Automatic registration of pelvic computed tomography data and magnetic resonance scans including a full circle method for quantitative accuracy evaluation. Med Phys 2002;25:2054–67.
[33] Schaake EE, Rossi MMG, Buikhuisen WA, Burgers JA, Smit AAJ, Belderbos JSA, et al. Differential motion between mediastinal lymph nodes and primary tumor in radically irradiated lung cancer patients. Int J Radiat Oncol Biol Phys 2014;90:959–66.
[34] Brock KK. Results of a Multi-Institution Deformable Registration Accuracy Study (MIDRAS). Int J Radiat Oncol Biol Phys 2010;76:583–96.
[35] van de Lindt TN, Schubert G, van der Heide UA, Sonke JJ. An MRI-based mid-ventilation approach for radiotherapy of the liver. Radiother Oncol 2016;121:276–80.
[36] Van Herk M. Errors and margins in radiotherapy. Semin Radiat Oncol 2004;14:52–64.
[37] Fast M, van de Schoot A, van de Lindt T, Carbaat C, van der Heide U, Sonke JJ. Tumor trailing for liver SBRT on the MR-linac. Int J Radiat Oncol Biol Phys 2019;103:468–78.